PCCP

ROYAL SOCIETY OF CHEMISTRY

PAPER

View Article Online
View Journal | View Issue

Cite this: *Phys. Chem. Chem. Phys.*, 2026, **28**, 2072

Impact of fluorine substitution position on triarylamine-based hole transport materials in perovskite solar cells

Bhim Raju Telugu,*[a] Hanbo Jung,[ab] Zhanglin Guo [abc] and Toshinori Matsushima *[abcd]

The molecular engineering of organic hole-transporting materials (HTMs) plays a crucial role in enhancing both the performance and stability of perovskite solar cells (PSCs). In this study, we investigated the impact of fluorine (F) substitution at different positions (*ortho* or *meta*) on the triarylamine donor unit connected to a benzo[1,2-*b*:4,5-*b*′]dithiophene (BDT) core. Four donor–π–donor type HTMs were designed and synthesized: BDT-NoF [4,4′-(benzo[1,2-*b*:4,5-*b*′]dithiophene-2,6-diyl)bis(*N*,*N*-bis(4-methoxyphenyl)aniline)], BDT-mF [4,4′-(benzo[1,2-*b*:4,5-*b*′]dithiophene-2,6-diyl)bis(2-fluoro-*N*,*N*-bis(4-methoxyphenyl)aniline)], BDT-OF [4,4′-(benzo[1,2-*b*:4,5-*b*′]dithiophene-2,6-diyl)bis(3-fluoro-*N*,*N*-bis(4-methoxyphenyl)aniline)], and BDT-OF-Flu [*N*,*N*′-(benzo[1,2-*b*:4,5-*b*′]dithiophene-2,6-diylbis(2-fluoro-4,1-phenylene))bis(*N*-(4-methoxyphenyl)-9,9-dimethyl-9*H*-fluoren-2-amine)]. The chemical structures, optical and electrochemical properties, film morphologies, and device performances of these HTMs were thoroughly characterized. The positional variation of the fluorine substituents induced distinct intramolecular noncovalent interactions that influenced the optoelectronic behavior and charge-transport properties. Devices employing BDT-NoF, BDT-mF, BDT-OF and BDT-OF-Flu achieved average power conversion efficiencies (PCEs) of 14.9%, 12.4%, 16.7%, and 8.0%, respectively. Notably, BDT-OF exhibited the highest power conversion efficiency (16.7%), among the series, due to favorable packing characteristics, promoting pinhole-free film formation and efficient charge extraction. These findings indicate that position of fluorine substitution and the choice of terminal aryl group significantly affect the energy-level alignment, molecular packing, and interfacial contact with the perovskite layer. This study provides valuable insights into the rational molecular design of HTMs, emphasizing the importance of fluorine positioning and structural engineering for optimizing PSC efficiency and stability.

Received 24th October 2025,
Accepted 19th December 2025

DOI: 10.1039/d5cp04078g

rsc.li/pccp

1 Introduction

Over the past decade, perovskite solar cells (PSCs) have emerged as one of the most promising photovoltaic technologies, demonstrating remarkable progress in power conversion efficiency (PCE) that rivals crystalline silicon solar cells. The PCE of PSCs has increased from 3.8% in 2009 to 27% for single-junction devices and 34.9% for perovskite/silicon tandem configurations.[1] PSCs offer numerous advantages, including facile solution-based fabrication processes, low production costs, tunable optoelectronic properties, and high defect tolerance. However, despite these impressive efficiency gains, the long-term operational stability of PSCs remains a critical obstacle to their widespread commercialization, particularly in outdoor environments.[2] Various extrinsic factors—such as exposure to ultraviolet (UV) light, moisture, oxygen, and elevated temperatures—lead to device degradation.[3] To overcome these challenges without compromising device performance, considerable efforts have been devoted to strategies such as device architecture optimization, interface engineering, and the development of advanced hole-transporting materials (HTMs).[4,5] Among these, HTMs play a pivotal role in PSCs by enabling efficient hole extraction from the perovskite layer to the metal electrode, improving interfacial contact, and providing favorable energy-level alignment. Furthermore, HTMs can function as protective layers, shielding the perovskite film from ambient oxygen and moisture, thereby enhancing overall device stability.[6–9]

[a] *International Institute for Carbon-Neutral Energy Research (WPI-I2CNER), Kyushu University, Fukuoka 819-0395, Japan. E-mail: tmatusim@i2cner.kyushu-u.ac.jp*
[b] *Center for Energy Systems Design (CESD), International Institute for Carbon-Neutral Energy Research (WPI-I2CNER), Kyushu University, Fukuoka 819-0395, Japan*
[c] *Department of Automotive Science, Graduates School of Integrated Frontier Sciences, Kyushu University, 744 Motooka, Nishi, Fukuoka 819-0395, Japan*
[d] *Department of Applied Chemistry, Faculty of Engineering, Kyushu University, Fukuoka 819-0395, Japan*

From last decade, detailed investigations on HTMs, including small organic compounds, inorganic compounds,[10] polymeric materials,[11,12] and metal–organic compounds,[13] have been extensively reported. The key design strategies for effective HTMs include the following: (i) a donor–acceptor (D–A) structure typically exhibits a large dipole moment and strong intramolecular charge-transfer (CT) characteristics. These properties enhance intermolecular interactions and facilitate both charge separation and hole transport. (ii) A planar π-conjugated system is preferred for high charge-carrier mobility, as it tends to form ordered molecular packing, thereby enhancing intermolecular π–π interactions. This close packing not only promotes efficient hole transport but also suppresses ionic interdiffusion and improves photostability in planar HTM-based devices. (iii) HTMs contain functional groups with lone pair electrons, which act as defect (especially undercoordinated Pb^{2+}) passivation on top of the perovskite through Lewis acid–base interaction. These functional groups inhibit ion migration, resulting in more efficient charge extraction and transfer at interfaces with reduced interfacial recombination losses. This represents a crucial strategy for enhancing PSC performance. Therefore, the incorporation of electron-rich functional groups or aromatic units, structural optimization (*e.g.*, energy level tuning), and precise control of molecular packing and intermolecular interactions are highly desirable for the development of high-performance HTMs.[6–9]

Recently, noncovalent conformational locks have been successfully employed to design and synthesize highly planar D–π–D conjugated organic HTMs.[14–23] These HTMs, owing to their high hole mobility and ability to form smooth and uniform films, contribute to improved PCE and exhibit excellent thermal stability. Fluorine (F) substitution in organic HTMs is known to induce strong intermolecular noncovalent interactions and enhance moisture resistance, particularly in conventional (n–i–p) device architectures. Additionally, F substitution serves as an effective strategy for tuning optoelectronic properties and molecular planarity through noncovalent interactions such as F···H and F···S with neighboring thiophene units. These interactions reduce the dihedral angle (θ), thereby improving crystallinity, charge transport, and the film-forming properties of the HTMs. Furthermore, fluorinated HTMs exhibit higher polarization and a reduced coulombic potential between holes and electrons. The incorporation of F substituents into 4-methoxy-*N*-(4-methoxyphenyl)-*N*-phenylaniline (MeOTPA)-based HTMs has been widely adopted to enhance photovoltaic performance and improve the environmental stability of PSCs.[14–23]

The energy levels, molecular packing, hole mobility, and other key properties of HTMs can be effectively tuned by modifying the terminal aromatic units. Recently, various conjugated moieties and structural analogues of 2,2′,7,7′-tetrakis-(*N*,*N*-di-4-methoxyphenylamino)-9,9′-spirobifluorene (spiro-OMeTAD) or other spiro-type HTMs have been reported. For example, J. Manit *et al.* developed a spiro[fluorene-9,9′-xanthene] (SFX) core with carbazole motifs as peripheral substituents (XC2-M), achieving a PCE of 11.4%.[24] Similarly, D. Zhang *et al.* reported SFX-based HTMs with end-capped π-conjugated anthracene (X87) and phenanthrene (X84) units; the X87-based PSCs achieved a high PCE of 24.07% along with exceptional long-term operational stability.[25] Z. Zhang *et al.* further explored halogen-substituted SFX-type HTMs, such as mF-SFXDA and mCl-SFXDA, which exhibited PCEs of 21.83% and 22.14%, respectively.[17] These improvements are attributed to the isotropic coordination capability of the halogen atoms with Pb^{2+} at the perovskite surface. In another approach, modifications were made to the spiro-OMeTAD structure by replacing one of its methoxyphenyl terminal groups. M. Jeong *et al.* introduced fluorine atoms into the spiro-OMeTAD framework, yielding two fluorinated isomers, spiro-mF and spiro-oF. The strong electron-withdrawing nature of fluorine induced deeper HOMO levels and altered the dihedral angles, resulting in enhanced device performance. Devices incorporating spiro-mF and spiro-oF achieved PCEs of 24.64% and 22.31%, respectively.[18] Similarly, X. Liu *et al.* developed spiro-mCl by introducing a chlorine atom, achieving the highest reported PCE of 25.26% among spiro derivatives.[26] X. Zhang *et al.* substituted a phenyl methylthio group into spiro-OMeTAD, creating spiro-SMeTAD and spiro-OSMeTAD. They found that the HTM with mixed terminal groups—half methoxy and half methylsulfanyl (spiro-OSMeTAD)—exhibited superior device performance and reduced hysteresis compared to the all-methoxy (spiro-OMeTAD) and all-methylsulfanyl (spiro-SMeTAD) analogues. This improvement was attributed to better film-forming properties and more efficient hole extraction.[27] N. J. Jeon and co-workers developed a spiro-type HTM (DM) by replacing one methoxyphenyl group with a 9,9′-dimethylfluorene moiety. Although DM-based devices showed a slightly lower PCE of 22.91% compared to spiro-OMeTAD (23.05%), they demonstrated improved stability.[28] Z. Deng and co-workers also modified the spiro-OMeTAD structure by substituting one 4-methoxyphenyl group with *N*-ethylcarbazole or dibenzothiophene, creating HTMs named SC and ST, respectively. SC exhibited good solubility and amorphous nature due to the presence of an internal ethyl chain, which helped suppress unfavorable phase separation. As a result, SC-based devices achieved a PCE of 21.76%, outperforming spiro-OMeTAD-based devices (20.73%).[29] Despite these developments, doped spiro-OMeTAD remains the most widely used HTM for high-efficiency n–i–p structured PSCs. However, it suffers from several inherent limitations. Its complex synthesis and purification steps and high production cost hinder large-scale commercialization. Furthermore, the spiro configuration leads to weak intermolecular interactions, resulting in thick HTM layers with low intrinsic hole mobility and poor thermal stability. To address these challenges, extensive research has been directed toward developing cost-effective HTMs with improved intrinsic hole mobility and stronger intermolecular interactions.

In this work, we investigated the effect of *ortho*- and *meta*-fluorine (F) substitutions on triarylamine donor units within donor–π–donor (D–π–D) structured HTMs, and systematically examined their influence on PSC performance. An electron-rich fused heterocyclic unit, benzo[1,2-*b*:4,5-*b*′]dithiophene (BDT), was employed as the central π-bridge in the HTM design due to its high hole mobility, multiple functionalization sites, and

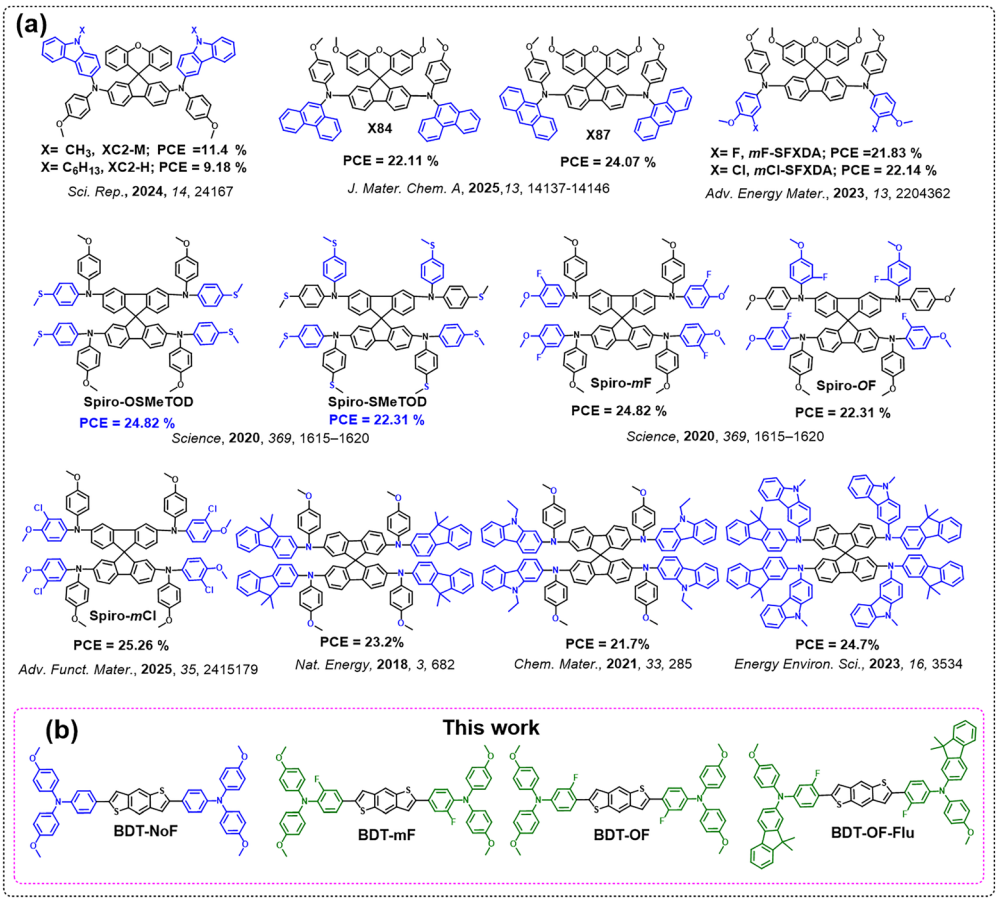

Fig. 1 (a) Recent developments in small-molecule HTMs with diverse terminal groups employed in n–i–p structured PSCs. (b) Chemical structures of the HTMs reported in this work.

excellent defect passivation properties.[30–32] Four HTMs—BDT-NoF, BDT-mF, BDT-OF, and BDT-OF-Flu—were synthesized by systematically modifying the donor moiety with or without F substitution (see Fig. 1(b)). Compared to BDT-NoF, the F-containing HTMs (BDT-mF, BDT-OF, and BDT-OF-Flu) exhibit deeper HOMO energy levels, attributed to the electron-withdrawing nature of the F atom. Furthermore, the introduction of F atoms induces multiple intra- and intermolecular interactions, including F···S and F···H (C–H/π) contacts, which enhance molecular planarity, facilitate intramolecular charge delocalization, and influence π–π stacking. Notably, the *meta*-F-substituted HTM (BDT-mF) exhibits a larger dihedral angle than its *ortho*-F analogues (BDT-OF and BDT-OF-Flu), leading to looser molecular packing. By contrast, BDT-OF and BDT-OF-Flu films are likely to display more compact π–π stacking than those based on BDT-NoF and BDT-mF. The corresponding PSCs fabricated with BDT-NoF, BDT-mF, BDT-OF, and BDT-OF-Flu achieved average PCEs of 14.9%, 12.4%, 16.7%, and 8.0%, respectively. These results indicate that structural optimization through terminal group modification or fluorine substitution at different positions of the triarylamine unit can markedly influence film formation, charge transport, and electron delocalization, thereby enhancing device performance.

2 Results and discussion

The synthetic routes of the HTMs are illustrated in Fig. S1, with detailed procedures provided in the SI. All intermediates, including 4-bromo-3-fluoro-*N*,*N*-bis(4-methoxyphenyl)aniline, 4-bromo-2-fluoro-*N*,*N*-bis(4-methoxyphenyl)aniline, and *N*-(2-fluorophenyl)-*N*-(4-methoxyphenyl)-9,9-dimethyl-9*H*-fluoren-2-amine, were synthesized *via* the Buchwald–Hartwig amination method. The target HTMs were subsequently prepared through palladium-catalyzed Suzuki–Miyaura coupling reactions using tetrakis(triphenylphosphine)palladium(0) ($Pd(PPh_3)_4$) as the catalyst. The chemical structures of all synthesized HTMs were thoroughly characterized by proton nuclear magnetic resonance spectroscopy (^{1}H NMR), carbon-13 nuclear magnetic resonance spectroscopy (^{13}C NMR), and matrix-assisted laser desorption/ionization time-of-flight/time-of-flight mass spectrometry (MALDI-TOF/TOF), as detailed in the SI (Fig. S1–S25).

The UV-Vis absorption spectra of HTMs were recorded in chloroform to evaluate their photophysical properties, with the corresponding data summarized in Table 1. All HTMs exhibit two absorption bands in the range of 250–350 and 350–500 nm, which can be attributed to the π–π* transition and intramolecular charge transfer (ICT), respectively. The strong ICT absorption observed between 350–500 nm arises from charge

Table 1 Optical and electronic properties of the HTMs

HTM	Absorption maximum (nm)		$\varepsilon_{max,solution}$ (M^{-1} cm^{-1})	λ_{onset} in film (nm)	$E_g^{opt\,c}$ (eV)	Energy levels (eV)	
	Solution[a]	Film[b]				HOMO[d]	LUMO[e]
BDT-NoF	410	416	16 000	480	2.58	−5.28	−2.70
BDT-mF	412	420	17 500	482	2.57	−5.39	−2.82
BDT-OF	405	410	19 100	470	2.63	−5.40	−2.77
BDT-OF-Flu	412	414	28 400	475	2.61	−5.47	−2.86

[a] Absorption spectra measured in chloroform. [b] Thin films fabricated by spin-coating from solutions with 60 mg mL^{-1}. [c] The optical bandgap was obtained from $E_g^{opt} = 1240/\lambda_{onset}$. [d] The HOMO level estimated form CV. [e] The LUMO level estimated with $E_{HOMO} - E_g^{opt}$.

transfer between the terminal triarylamine units and the central π-conjugated BDT core. Compared to their solution-state spectra, the absorption peaks in the thin films are partially red-shifted, indicating enhanced π–π interactions in the solid state. As shown in Fig. 2(a) and (b), the main absorption peaks (λ_{max}) in solution/film for the undoped BDT-NoF, BDT-mF, BDT-OF, and BDT-OF-Flu HTMs are observed at 410/416, 412/420, 405/410, and 412/414 nm, respectively. Notably, BDT-OF and BDT-OF-Flu (fluorene substitution) exhibit smaller red shifts upon film formation than BDT-NoF and BDT-mF, suggesting that the *ortho*-F substitution promotes stronger intramolecular and intermolecular π–π interactions through favorable F···S or F···H (C–H/π) interactions with neighboring BDT cores. In particular, BDT-OF-Flu exhibits only a 2 nm red shift, likely attributable to the terminal fluorene units, which may promote more compact molecular packing in the solid state (as confirmed by scanning electron microscopy (SEM) images). The absorption onsets (λ_{onset}) of the undoped thin films for BDT-NoF, BDT-mF, BDT-OF, and BDT-OF-Flu are 480, 482, 470, and 475 nm, respectively, corresponding to optical bandgaps (E_g^{opt}) of 2.58, 2.57, 2.63, and 2.61 eV, calculated using the empirical relation $E_g^{opt} = 1240/\lambda_{onset}$. All relevant photophysical data are summarized in Table 1.

Moreover, the corresponding highest occupied molecular orbital (HOMO) energy levels of the HTMs were determined from the cyclic voltammetry (CV) measurements, as shown in Fig. 2(c) and summarized in Table 1. The HOMO levels were calculated to be −5.28, −5.39, −5.40, and −5.47 eV for BDT-NoF, BDT-mF, BDT-OF, and BDT-OF-Flu HTMs, respectively. These values are in close agreement with the valence band maximum of the triple-cation perovskite $Cs_{0.05}(FA_{0.85}MA_{0.15})_{0.95}Pb(I_{0.85}Br_{0.15})_3$ used later for the PSC fabrication (−5.43 eV), enabling favorable hole extraction from the perovskite to the HTMs, except in the case of BDT-OF-Flu, which shows a slightly deeper HOMO level at −5.47 eV.[33] The lowest unoccupied molecular orbital (LUMO) energy levels of the HTMs were then estimated using the empirical formula LUMO = HOMO − E_g^{opt}. Accordingly, the LUMO levels of BDT-NoF, BDT-mF, BDT-OF, and BDT-OF-Flu were estimated to be −2.70 eV, −2.82 eV, −2.77 eV, and −2.86 eV, respectively (see Fig. 2(d)). These LUMO values are significantly shallower than the conduction band minimum (CBM) of the perovskite

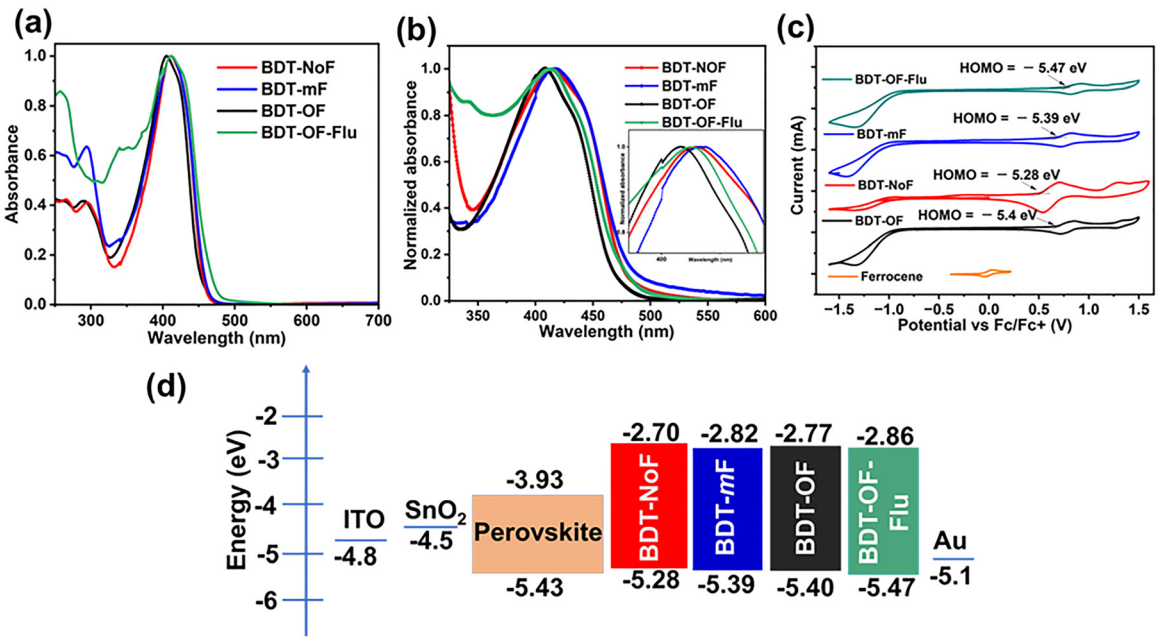

Fig. 2 (a) Normalized UV-Vis absorption spectra of the HTMs in chloroform solution. (b) Normalized UV-Vis absorption spectra of HTM thin films. (c) CV results of HTMs recorded in DCM. (d) Schematic energy-level diagram of PSCs incorporating the undoped HTMs.

(−3.93 eV), effectively preventing undesirable electron back-transfer from the HTM to the perovskite.

Subsequently, density functional theory (DFT) calculations were performed using the B3LYP/6-31G(d,p) basis set to provide insights into the molecular geometries, frontier molecular orbital (FMO) energy levels, and dipole moments of the four HTMs. As shown in Fig. 3, all HTMs exhibit planar conformations. Notably, the insertion of *ortho* F atoms on the triarylamine core leads to decreased dihedral angles. Consequently, BDT-OF and BDT-OF-Flu promote greater backbone coplanarity, which should be beneficial for ICT from the donor to the π-linker. Moreover, as illustrated in Fig. 3, the HOMOs of BDT-NoF, BDT-mF, and BDT-OF are delocalized across the entire molecule, spanning from the central π-core to the triphenylamine moieties. In contrast, the HOMO of BDT-OF-Flu is not distributed over the terminal fluorene unit, which may hinder efficient charge transport from the terminal group to the π-core (as evidenced by the device results). In all HTMs, the LUMOs are mainly localized on the central BDT bridge. The HOMO and LUMO energy levels estimated by DFT for BDT-NoF, BDT-mF, BDT-OF, and BDT-OF-Flu are −4.26/−1.32, −4.38/−1.50, −4.33/−1.34, and −4.34/−1.40 eV, respectively (Fig. 3). Additionally, among the investigated molecules, BDT-OF-Flu (μ = 0.283 D) exhibits a significantly higher dipole moment than BDT-NoF (μ = 0.020 D), BDT-mF (μ = 0.069 D), and BDT-OF (μ = 0.011 D).

The surface morphology of HTM layers plays a critical role in determining the photovoltaic performance of PSCs. To examine the surface morphology, scanning electron microscopy (SEM) was conducted on chemically doped HTM layers deposited atop the triple-cation perovskite layer (Fig. 4). The incorporation of the BDT linker into the triarylamine core effectively suppresses film aggregation and promotes the formation of smooth films. Such smooth films are beneficial for efficient hole extraction from the perovskite layer, thereby enhancing PCE. Although BDT-NoF and BDT-mF share similar backbone architectures, their films display limited π–π stacking and the formation of pinholes, both of which can impede efficient charge transport (see the electrical conductivity measurements discussed later). In contrast, *ortho*-fluorine-substituted HTMs, such as BDT-OF and BDT-OF-Flu, can engage in non-covalent interactions (F···S and F···H), yielding homogeneous, pinhole-free films with enhanced π–π stacking.[20] These high-quality films minimize charge transport losses and improve interfacial contact at the perovskite/HTM/electrode interfaces, ultimately contributing to improved device performance.

The PSCs were fabricated with a conventional device configuration of glass substrate/indium tin oxide (ITO; 150 nm)/SnO_2 (30 nm)/$Cs_{0.05}(FA_{0.85}MA_{0.15})_{0.95}Pb(I_{0.85}Br_{0.15})_3$ (650 nm)/HTM layer/Au (80 nm), as illustrated in Fig. 5(a), and the corresponding photovoltaic data in average are summarized in Table 2. Details of the device fabrication processes are provided in the SI. All experimental results are summarized in Tables S1–S5. Fig. 5(b) presents the current density–voltage (*J–V*) curves of representative devices, recorded under AM 1.5G simulated illumination at an intensity of 100 mW cm^{-2}. Devices incorporating BDT-OF as the HTM achieved a high PCE of 16.7%, with a V_{OC} of 1.02 V, a J_{SC} of 23.1 mA cm^{-2}, and an FF of 0.70, with reduced hysteresis (Fig. S26 and Table S6). This enhancement is attributed due to the better alignment of the HOMO level with the perovskite's valence band (see Fig. 2(d)), as well as strong π–π intermolecular interactions that improve charge transport properties. In contrast, the structurally similar BDT-OF-Flu, which incorporates terminal fluorene groups, exhibited poor device performance, yielding a PCE of 8.05%, with a V_{OC} of 0.87 V, a J_{SC} of 23.7 mA cm^{-2}, and an FF of 0.38. The diminished performance is likely due to the partial

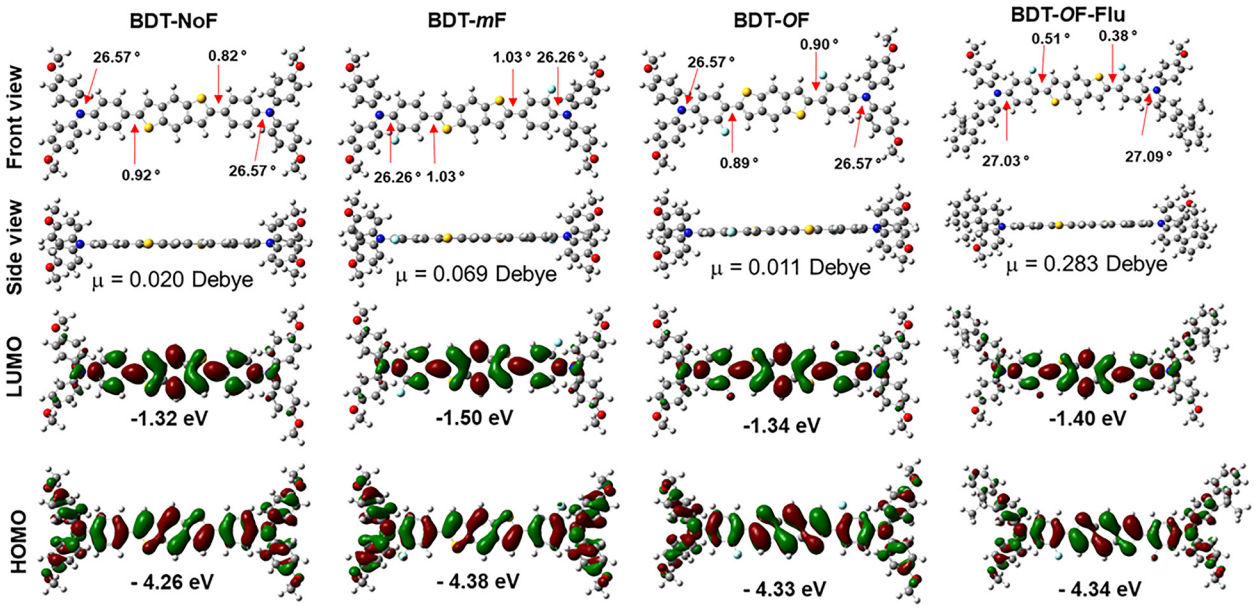

Fig. 3 DFT-optimized molecular geometries of the HTMs showing top and side views, along with the spatial distributions of the HOMO and LUMO orbitals and their corresponding energy levels, dipole moments and dihedral angles. Calculations were performed at the B3LYP/6-31G(d,p) level.

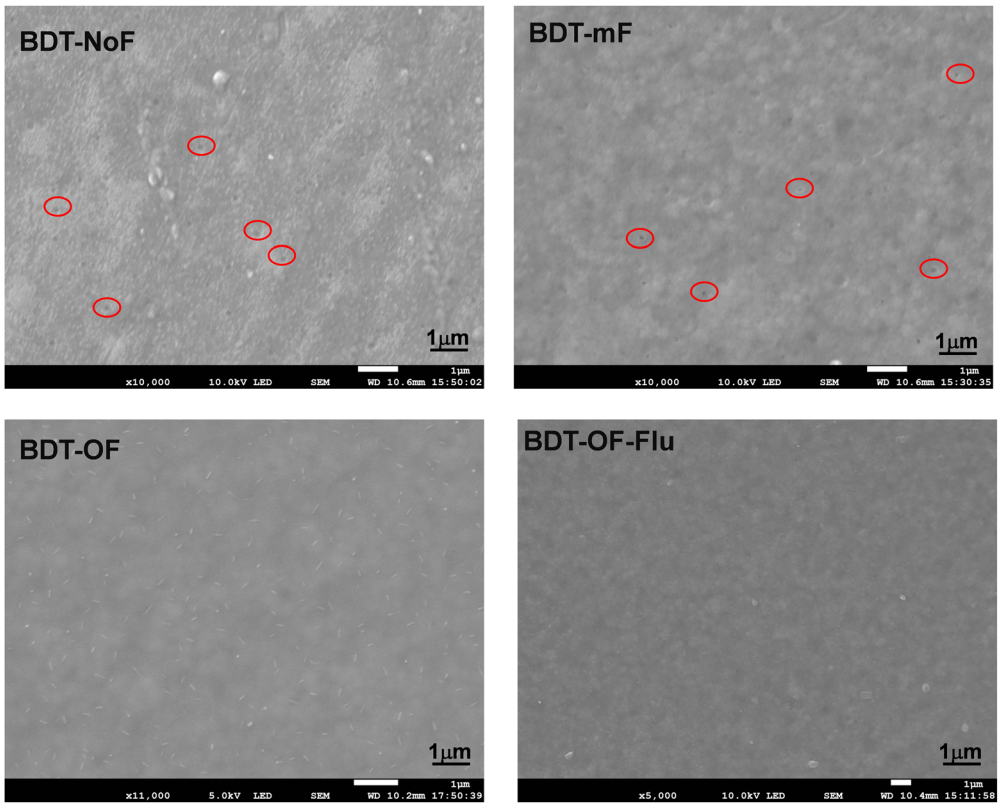

Fig. 4 Top-view SEM images of the doped HTM layers. Each image represents a 1-μm field of view, and pinholes are highlighted by red circles.

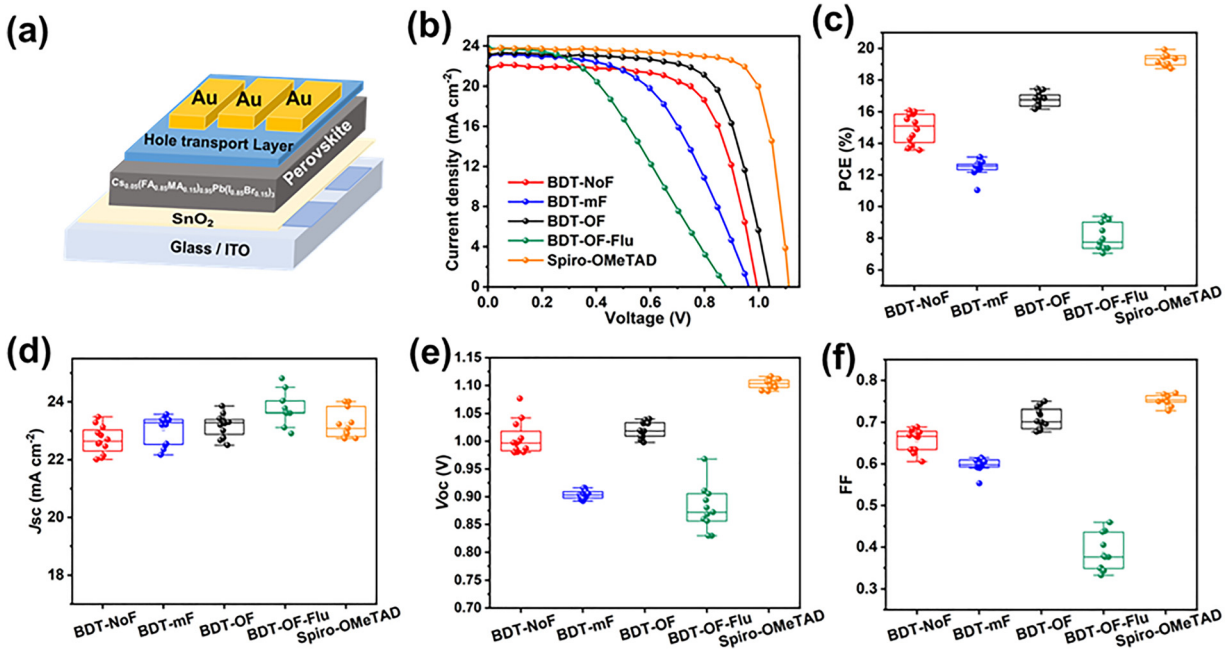

Fig. 5 (a) Schematic illustration of the PSC architecture incorporating HTMs. (b) Representative *J*–*V* curves of the devices measured under AM 1.5G illumination at 100 mW cm^{-2}. (c)–(f) Statistical distributions of photovoltaic parameters for the PSCs (average of 12 cells for each architecture).

distribution of the HOMO (see Gaussian data), which hampers ICT from the donor to the BDT core. Furthermore, the deep HOMO level (−5.47 eV) of BDT-OF-Flu may facilitate increased charge recombination and reduced hole extraction in the PSC

Table 2 Summary of the average values and standard deviations of J_{SC}, V_{OC}, FF, and PCE for doped HTMs in triple-cation-based PSCs

HTM	J_{SC} (mA cm^{-2})	V_{OC} (V)	FF	PCE (%)
BDT-NoF	22.6 ± 0.4	1.00 ± 0.04	0.65 ± 0.02	14.9 ± 0.9
BDT-mF	23.0 ± 0.4	0.90 ± 0.01	0.59 ± 0.01	12.4 ± 0.5
BDT-OF	23.1 ± 0.2	1.02 ± 0.01	0.70 ± 0.02	16.7 ± 0.4
BDT-OF-Flu	23.7 ± 0.5	0.87 ± 0.03	0.38 ± 0.04	8.05 ± 0.8
Spiro-OMeTAD	23.2 ± 0.5	1.10 ± 0.01	0.75 ± 0.01	19.2 ± 0.3

via back electron transport.[33] The introduction of *meta*-F on the triphenylamine groups in BDT-mF resulted in a moderate PCE of 12.4%, with a V_{OC} of 0.90 V, a J_{SC} of 23.0 mA cm^{-2}, and an FF of 0.59. In comparison, BDT-NoF, without F substitution, achieved a higher PCE of 14.9%, with a V_{OC} of 1.00 V, a J_{SC} of 22.6 mA cm^{-2}, and an FF of 0.65. For slandered reference, spiro-OMeTAD based devices was evaluated and it shows PCE of 19.2%, with a V_{OC} of 1.10 V, a J_{SC} of 23.2 mA cm^{-2}, and an FF of 0.75.

The lower PCE of BDT-mF might be due to weak molecular packing and higher dihedral angle between the donor and BDT core. These results clearly demonstrate that the position of F and the nature of the terminal aryl group in the donor unit effectively tune the energy levels of the HTM layer. Moreover, optimized energy-level alignment minimizes charge-carrier transport losses, further contributing to enhanced PCE. Compared to *meta*-F, *ortho*-F substitution in the triphenylamine donor promotes stronger molecular packing atop the perovskite layer, facilitating pinhole-free, efficient charge transport.

The electrical conductivity of the HTM layer plays a crucial role in PSCs, as it governs the efficient extraction of holes from the perovskite layer and their subsequent transport to the metal electrode, thereby directly influencing both the PCE and the overall device performance. The conductivity was evaluated using the following device configuration: glass substrate/ITO (≈100 nm)/chemically doped HTM layer/MoO_3 (10 nm)/Al (≈100 nm).[34,35] The thicknesses of the HTM layers, measured by laser microscopy, were ≈199 nm (BDT-NoF), ≈200 nm (BDT-mF), ≈150 nm (BDT-OF), and ≈230 nm (BDT-OF-Flu). The dark *J*–*V* curves of these devices are shown in Fig. 6(a). For the chemically doped HTM layers, the conductivities were 2.8×10^{-3} S cm^{-1} for BDT-NoF, 5.9×10^{-3} S cm^{-1} for BDT-mF, 7.0×10^{-3} S cm^{-1} for BDT-OF, and 6.3×10^{-3} S cm^{-1} for BDT-OF-Flu. All samples exhibited relatively high conductivities; however, no clear correlation with PSC performance was observed. This discrepancy likely arises because the device characteristics are governed not only by bulk hole transport within the HTM layer, but also by interfacial hole extraction, which depends strongly on energy-level alignment. However, BDT-OF demonstrates the highest electrical conductivity along with well-aligned energy levels, factors that likely underpin its superior device performance.

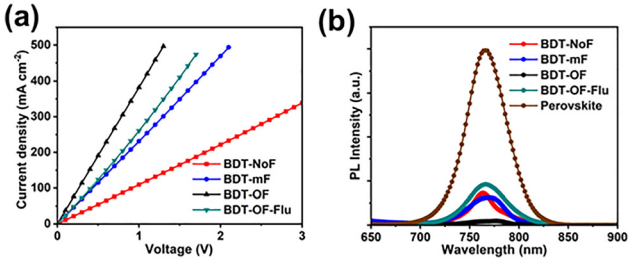

Fig. 6 (a) Representative *J*–*V* curves of chemically doped HTM devices. (b) Steady-state PL spectra of the perovskite layer with and without the HTM, indicating hole extraction efficiency.

To further investigate the hole extraction capabilities of the BDT-based HTMs, samples with the structure of fused silica substrate/perovskite/HTM (doped) were fabricated and analyzed using steady-state photoluminescence (PL) measurements. As shown in Fig. 6(b), PL spectra were recorded for perovskite films coated with various doped HTM layers upon excitation at 380 nm, with all samples exhibiting an emission peak at 775 nm. A significant quenching of the PL signal was observed upon HTM layer deposition, indicating efficient hole extraction at the perovskite/HTM layer interface. The PL quenching efficiency, reflected by the decrease in PL intensity, followed the trend: BDT-OF-Flu (76.9%) < BDT-NoF (81.7%) < BDT-mF (84.5%) < BDT-OF (97.1%). Except for BDT-OF, the use of other HTMs resulted in weaker PL quenching, suggesting less efficient hole extraction at the perovskite/HTM interface. Notably, the extent of PL quenching correlates not only with the energy-level alignment of the HTMs but also with their intrinsic bulk hole-transport properties, closely mirroring the observed trends in solar cell performance.

PSCs employing spiro-OMeTAD, BDT-NoF, and BDT-OF as HTM layers exhibited a very rapid photoresponse; the PCE reached its maximum value within a few seconds of light illumination. These devices also showed well-behaved incident photon-to-current efficiency (IPCE) spectra, predominantly confined to wavelengths below 800 nm (Fig. S27).

Finally, the thermal properties of the BDT-NoF and BDT-OF HTMs were evaluated using thermogravimetric analysis (TGA) and differential scanning calorimetry (DSC), as shown in Fig. S28. In general, TGA curves reveal weight loss arising from thermal events such as volatilization, decomposition, or phase transitions. BDT-NoF and BDT-OF exhibit decomposition temperatures of 371 °C and 392 °C, respectively, demonstrating their high thermal stability. Such robust thermal resilience is advantageous for PSC applications.

3 Conclusion

In conclusion, we successfully synthesized four D–π–D structured HTMs—BDT-NoF, BDT-mF, BDT-OF, and BDT-OF-Flu—by systematically tailoring the donor units to modulate their optical and electrochemical properties. This study presents a rational molecular design strategy to enhance HTM performance in PSCs through targeted structural modifications. Amid the rapid development of numerous functional organic materials for PSC applications,[36–42] these results offer meaningful guidance for future material design. Among these, BDT-OF, incorporating *ortho*-fluorine substitution, exhibited well-aligned energy levels,

enhanced interfacial interactions with the perovskite layer, and superior film morphology. As a result, PSCs based on BDT-OF delivered a PCE of 16.3%, surpassing those based on BDT-mF (12.0%), BDT-OF-Flu (8.05%), and BDT-NoF (14.1%). These results iindicate the critical role of fluorine substitution position and terminal aryl group modification in fine-tuning HTM energy levels and morphology. Moreover, optimized energy alignment mitigates charge-transport losses, thereby contributing to higher PCE. In particular, *ortho*-fluorine substitution on the triphenylamine donor facilitates favorable molecular packing atop the perovskite layer, yielding pinhole-free films and efficient charge transport.

Author contributions

T. B. R. conducted the synthesis, device fabrication, evaluation, and data analysis under the supervision of T. M., while H. J., and Z. G. provided support with instrumentation. All authors reviewed and approved the final manuscript.

Conflicts of interest

There are no conflicts to declare.

Data availability

The data that support the findings of this study are available from the corresponding author upon reasonable request.

Supplementary information (SI) is available. See DOI: https://doi.org/10.1039/d5cp04078g.

Acknowledgements

This work was supported by Mitsui Chemicals, Inc.— Carbon Neutral Research Center (MCI-CNRC), I2CNER, Kyushu Univ.; New Energy and Industrial Technology Development Organization (NEDO), the Green Innovation Fund Project (grant number 21578635); Science and Technology Research Partnership for Sustainable Development (SATREPS), Japan Science and Technology Agency (JST) (grant number JPMJSA2306); Precursory Research for Embryonic Science and Technology (PRESTO), JST (grant number JPMJPR23H8); ASPIRE FOR RISING SCIENTISTS, Adopting Sustainable Partnerships for Innovative Research Ecosystem (ASPIRE), JST (grant number JPMJAP2332); JSPS KAKENHI (grant numbers 20H02817 and 24H00486); the Iwatani Naoji Foundation; and the Asahi Glass Foundation.

References

1 A. Kojima, K. Teshima, Y. Shirai and T. Miyasaka, *J. Am. Chem. Soc.*, 2009, **131**, 6050–6051.
2 C. C. Boyd, R. Cheacharoen, T. Leijtens and M. D. McGehee, *Chem. Rev.*, 2019, **119**, 3418–3451.
3 B. P. Kore, M. Jamshidi and J. M. Gardner, *Mater. Adv.*, 2024, **5**, 2200–2217.
4 S. Mariotti, E. Köhnen, F. Scheler, K. Sveinbjörnsson, L. Zimmermann, M. Piot, F. Yang, B. Li, J. Warby, A. Musiienko, D. Menzel, F. Lang, S. Keßler, I. Levine, D. Mantione, A. Al-Ashouri, M. S. Härtel, K. Xu, A. Cruz, J. Kurpiers, P. Wagner, H. Köbler, J. Li, A. Magomedov, D. Mecerreyes, E. Unger, A. Abate, M. Stolterfoht, B. Stannowski, R. Schlatmann, L. Korte and S. Albrecht, *Science*, 2023, **381**, 63–69.
5 C. Liu, Y. Yang, H. Chen, J. Xu, A. Liu, A. S. R. Bati, H. Zhu, L. Grater, S. Sudhakar Hadke, C. Huang, V. K. Sangwan, T. Cai, D. Shin, L. X. Chen, M. C. Hersam, C. A. Mirkin, B. Chen, M. G. Kanatzidis and E. H. Sargent, *Science*, 2023, **382**, 810–815.
6 C. Zhang, K. Wei, J. Hu, X. Cai, G. Du, J. Deng, Z. Luo, X. Zhang, Y. Wang, L. Yang and J. Zhang, *Mater. Today*, 2023, **67**, 518–547.
7 W. Wang, J. Zhou and W. Tang, *J. Mater. Chem. A*, 2022, **10**, 1150–1178.
8 A. Farokhi, H. Shahroosvand, G. D. Monache, M. Pilkington and M. K. Nazeeruddin, *Chem. Soc. Rev.*, 2022, **51**, 5974–6064.
9 X. Yin, Z. Song, Z. Li and W. Tang, *Energy Environ. Sci.*, 2020, **13**, 4057–4086.
10 Q. Wang, Z. Lin, J. Su, Z. Hu, J. Chang and Y. Hao, *Nano Select*, 2021, **2**, 1055–1080.
11 E. A. Komissarova, S. A. Kuklin, V. V. Ozerova, A. V. Maskaev, A. F. Akbulatov, N. A. Emelianov, A. V. Mumyatov, L. G. Gutsev, L. A. Frolova and P. A. Troshin, *ACS Appl. Energy Mater.*, 2025, **8**, 4072–4079.
12 S. Yin, X. Luo, F. Tang, W. Zhong, W. Yang, Z. Xiong, Y. Lin, F. Peng and L. Ying, *Adv. Energy Mater.*, 2025, **15**, 2404575.
13 Z. Yu, L. Wang, X. Mu, C. C. Chen, Y. Wu, J. Cao and Y. Tang, *Angew. Chem., Int. Ed.*, 2021, **60**, 6294–6299.
14 R. Li, J. Zhang, M. Liu, S. K. Matta, J. Tian, Z. Deng, S. P. Russo, P. Vivo, Z. Zhou and H. Zhang, *Sol. RRL*, 2023, **7**, 2300031.
15 G. B. Adugna, K. M. Lee, H. C. Hsieh, S. I. Lu, C. H. Lin, Y. C. Hsieh, J. H. Yang, J. M. Chiu, Y. S. Liu, C. W. Hu, W. H. Chiu, S. R. Li, K. L. Liau, Y. T. Tao and Y. D. Lin, *Sol. RRL*, 2024, **8**, 2300988.
16 G. B. Adugna, K. M. Lee, H. C. Hsieh, S. I. Lu, Y. C. Hsieh, J. H. Yang, W. H. Chiu, K. L. Liau, Y. T. Tao and Y. D. Lin, *Chem. Commun.*, 2023, **59**, 14653–14656.
17 Z. Zhang, L. Shen, S. Wang, L. Zheng, D. Li, Z. Li, Y. Xing, K. Guo, L. Xie and Z. Wei, *Adv. Energy Mater.*, 2023, **13**, 2204362.
18 M. Jeong, I. Woo Choi, E. Min Go, Y. Cho, M. Kim, B. Lee, S. Jeong, Y. Jo, H. Won Choi, J. Lee, J.-H. Bae, S. Kyu Kwak, D. Suk Kim and C. Yang, *Science*, 2020, **369**, 1615–1620.
19 K. Yang, Q. Liao, J. Huang, Z. Zhang, M. Su, Z. Chen, Z. Wu, D. Wang, Z. Lai, H. Y. Woo, Y. Cao, P. Gao and X. Guo, *Angew. Chem., Int. Ed.*, 2022, **61**, e202113749.
20 M. Zhai, N. Shibayama, T. B. Raju, T. Wu, C. Chen, Z. Guo, T. Matsushima, T. Miyasaka and M. Cheng, *Small*, 2025, **21**, 2505961.
21 T. B. Raju, C. A. M. Senevirathne, M. Watanabe, Y. Fujita, D. Senba and T. Matsushima, *J. Mater. Chem. C*, 2025, **13**, 15082–15090.

22 H. Zhang, X. Yu, M. Li, Z. Zhang, Z. Song, X. Zong, G. Duan, W. Zhang, C. Chen, W. H. Zhang, Y. Liu and M. Liang, *Angew. Chem., Int. Ed.*, 2023, **62**, e202314270.
23 G. Xie, Q. Xue, H. Ding, A. Liang, J. Liu, Y. Yang, J. Wang, X. Liao, Y. Min and Y. Chen, *Angew. Chem., Int. Ed.*, 2025, **64**, e202504144.
24 J. Manit, P. Kanjanaboos, P. Naweephattana, A. Naikaew, L. Srathongsian, C. Seriwattanachai, R. Supruangnet, H. Nakajima, U. Eiamprasert and S. Kiatisevi, *Sci. Rep.*, 2024, **14**, 24167.
25 D. Zhang, Q. Long, B. Sun, X. Luo, G. Zhou, J. Huang, Z. Zhang, J. Su and B. Xu, *J. Mater. Chem. A*, 2025, **13**, 14137–14146.
26 X. Liu, X. Zhang, Y. Zhou, W. Dai, J. Chen, O. A. Syzgantseva, M. A. Syzgantseva, B. Li, R. Ghadari, M. Han, W. Du, Z. Shao, Q. Wang, S. Dai, M. K. Nazeeruddin and Y. Ding, *Adv. Funct. Mater.*, 2025, **35**, 2415179.
27 X. Zhang, X. Liu, N. Wu, R. Ghadari, M. Han, Y. Wang, Y. Ding, M. Cai, Z. Qu and S. Dai, *J. Energy Chem.*, 2022, **67**, 19–26.
28 N. J. Jeon, H. Na, E. H. Jung, T. Y. Yang, Y. G. Lee, G. Kim, H. W. Shin, S. Il Seok, J. Lee and J. Seo, *Nat. Energy*, 2018, **3**, 682–689.
29 Z. Deng, M. He, Y. Zhang, F. Ullah, K. Ding, J. Liang, Z. Zhang, H. Xu, Y. Qiu, Z. Xie, T. Shan, Z. Chen, H. Zhong and C. C. Chen, *Chem. Mater.*, 2021, **33**, 285–297.
30 P. K. Vineetha, P. V. Nair, S. P. Sruthy and S. Anas, *Energy Technol.*, 2024, **12**, 2400591.
31 D. A. Ivanenko, O. I. Lashmanova, A. V. Sklemina, A. V. Skorlukhanova, M. M. Agapitova, A. N. Zhivchikova, M. M. Tepliakova, M. D. Tereshchenko, N. G. Nikitenko, A. A. Piryazev, E. D. Siaglova, D. A. Chernyayev, S. V. Karpov, I. E. Kuznetsov, D. A. Ivanov and A. V. Akkuratov, *Macromol. Chem. Phys.*, 2025, **226**, 2400489.
32 X. Kong, Y. Jiang, X. Wu, C. Chen, J. Guo, S. Liu, X. Gao, G. Zhou, J. M. Liu, K. Kempa and J. Gao, *J. Mater. Chem. A*, 2020, **8**, 1858–1864.
33 Y. Sun, Z. Wang, T. Geng, X. Liu, Y. Su, Y. Tian, M. Cheng and H. Li, *Materials*, 2025, **18**, 1400.
34 B. P.-Ochir, J. T. Song, P. Wang, M. Yahiro, S. Yamada, H. Nakanotani,T. Matsushima and C. Adachi, *Sol. RRL*, 2024, **8**, 2400029.
35 B. P.-Ochir, X. Liu, Y. Fujita, D. Semba, T. B. Raju, G. T.-Ulzii, A. Wachi, H. Sato, T. Matsushima and C. Adachi, *Sol. RRL*, 2023, **7**, 2300127.
36 K. Manda, V. D. Jadhav, P. Chetti, R. Gundla and S. Pola, *Org. Electron.*, 2025, **136**, 107153.
37 G. Maddala, R. Gade, J. Ahemed, S. Kalvapalli, N. B. Simhachalam, P. Chetti, S. Pola and R. Mitty, *Sol. Energy*, 2021, **226**, 501–512.
38 D. Bharath, M. Sasikumar, N. R. Chereddy, J. R. Vaidya and S. Pola, *Sol. Energy*, 2021, **174**, 130–138.
39 M. Sasikumar, G. Maddala, M. Ambapuram, M. Subburu, J. R. Vaidya, S. N. Babu, P. Chetti, R. Mitty and S. Pola, *Sustainable Energy Fuels*, 2020, **4**, 4754–4767.
40 Y. S. Lin, S. Y. Abate, K. W. Lai, C. W. Chu, Y. D. Lin, Y. T. Tao and S. S. Sun, *ACS Appl. Mater. Interfaces*, 2018, **10**, 41439–41449.
41 S. Venkateswarlu, Y.-D. Lin, K.-M. Lee, K.-L. Liau and Y.-T. Tao, *ACS Appl. Mater. Interfaces*, 2020, **12**(45), 50495–50504.
42 G. B. Adugna, S. Y. Abate, W.-T. Wu and Y.-T. Tao, *ACS Appl. Mater. Interfaces*, 2021, **13**(22), 25926–25936.

